ACS APPLIED ELECTRONIC MATERIALS

pubs.acs.org/acsaelm Article

Strain Relaxation via Phase Transformation in High-Mobility $SrSnO_3$ Films

Tristan K. Truttmann,* Fengdeng Liu, Javier Garcia-Barriocanal, Richard D. James, and Bharat Jalan*

Cite This: ACS Appl. Electron. Mater. 2021, 3, 1127−1132 Read Online

ACCESS | Metrics & More | Article Recommendations | Supporting Information

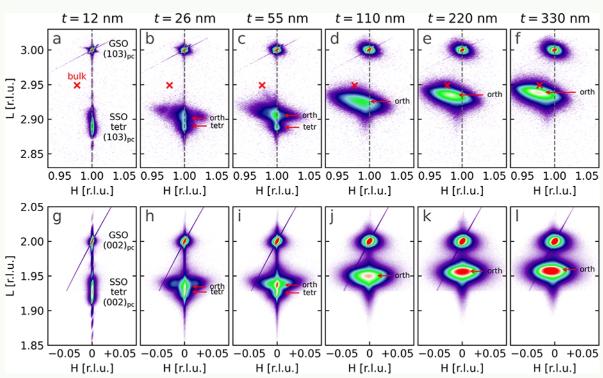

ABSTRACT: $SrSnO_3$ (SSO) is an emerging ultrawide band gap (UWBG) semiconductor with potential in high-power applications. In-plane compressive strain was recently shown to stabilize the high-temperature tetragonal phase of SSO at room temperature (RT), which exists at $T \geq 1062$ K in bulk. Here, we report on the study of strain relaxation in the epitaxial, tetragonal phase of Nd-doped SSO films grown on $GdScO_3$ (110) (GSO) substrates and how it influences the electronic transport properties. The thinnest SSO film (thickness, t = 12 nm) yielded a fully coherent tetragonal phase at RT. At 12 nm < t < 110 nm, the tetragonal phase first transformed into the orthorhombic phase, and then at $t \geq 110$ nm, the orthorhombic phase began to relax by forming misfit dislocations. Remarkably, the tetragonal phase remained fully coherent until it completely transformed into the orthorhombic phase. A significant increase in mobility from 14 to 73 $cm^2\ V^{-1}\ s^{-1}$ was discovered between 12 and 330 nm. Using thickness- and temperature-dependent electronic transport measurements, we discuss the important roles of the surface, phase coexistence, and misfit dislocations on carrier density and mobility in Nd-doped SSO. This study provides unprecedented insight into the effect of thickness and strain relaxation behavior and their consequences for electronic transport in doped SSO with implications for high-power electronic devices.

KEYWORDS: *perovskite oxides, stannates, octahedral rotations, strain engineering, strain relaxation, critical thickness, ultrawide band gap semiconductors*

■ INTRODUCTION

The family of perovskite alkaline-earth stannates has demonstrated room-temperature (RT) electron mobilities as high as 320 $cm^2\ V^{-1}\ s^{-1}$ in doped $BaSnO_3$ (BSO) bulk crystals,[1] a tunable band gap (indirect) from ∼3 eV in BSO to ∼4.1 eV in $SrSnO_3$ (SSO),[2−4] and even p-type doping.[5,6] In contrast to bulk single crystals, thin films of BSO have only achieved electron mobilities of 182 $cm^2\ V^{-1}\ s^{-1}$ at a carrier density of $1.2 \times 10^{20}\ cm^{-3}$.[7] This discrepancy in electron mobility between BSO films and bulk crystals is attributed largely to the presence of threading dislocations in thin films owing to the lack of commercially available lattice-matched substrates.[7−9] There are ongoing efforts toward the development of homoepitaxy,[10] buffer layers,[8,11] and lattice-matched substrates[6,12,13] to reduce the density of threading dislocations in BSO, but none of these efforts have yet resulted in electron mobilities that rival those in bulk single crystals. SSO is a non-cubic member of the stannate family. Similar to BSO, the SSO's conduction band is derived from Sn-5s orbitals and consequently has a low electron effective mass.[14−16] SSO can also be doped n-type with rare-earth elements and has demonstrated room-temperature electron mobilities as high as 70 $cm^2\ V^{-1}\ s^{-1}$ in thin films.[14,17−20] Unlike BSO, however, SSO has a wider band gap (∼4.1 eV),[2−4] which makes it more attractive as an ultrawide band gap (UWBG) semiconductor for power device applications.[21] Importantly, SSO can also be grown coherently on commercially available substrates due to its smaller lattice parameter that not only offers a path to avoid the threading dislocations, which have plagued BSO films, but also opens the door to strain engineering.[14,17] An earlier work from our group has shown that compressive epitaxial strain can stabilize the high-temperature tetragonal polymorph (T) of bulk SSO to below RT, more than 700 K below its stability range in bulk.[14] Films grown under no strain or tensile strain adopt the RT orthorhombic polymorph (O), as illustrated in Figure 1. However, it has yet to be understood how these phases evolve with increasing film thickness. For instance, will strain-stabilized tetragonal SSO on GSO (110) undergo a phase transition or will it form misfit dislocations if the film

Received: November 12, 2020
Accepted: February 15, 2021
Published: March 1, 2021

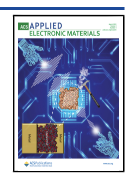

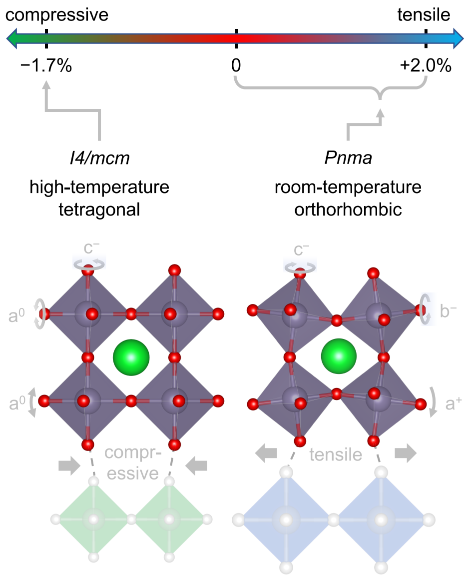

Figure 1. Schematic illustrating strain stabilization of SSO under compressive and tensile strain. Compressive strain stabilizes the tetragonal phase (*I*4/*mcm* with an $a^0a^0c^+$ tilt pattern), whereas no strain and tensile strain tend to stabilize a room-temperature orthorhombic phase (*Pnma* with an $a^+b^-c^-$ tilt pattern).

thickness is increased? It is also conceivable that the elastic strain energy can be accommodated through oxygen octahedral rotation/tilt,[22] polarization,[23] ferroelastic domain formation,[24] and/or structural phase transition.[25,26]

In this paper, we investigate strain relaxation in the strain-stabilized tetragonal phase of Nd-doped SSO films grown on GSO (110) substrates. We find that the phase transformation ($T \rightarrow O$) precedes strain relaxation via the formation of misfit dislocations with increasing film thickness. A significant increase in carrier density from 1.3×10^{18} to 1.3×10^{20} cm^{-3} was discovered accompanied by an increase in mobility from 14 to 73 $cm^2\ V^{-1}\ s^{-1}$ between 12 and 330 nm. Surprisingly, we found a conduction dead layer of 12 nm, below which films remain insulating despite a high doping concentration ($\sim 1.3 \times 10^{20}$ cm^{-3}). We discuss possible mechanisms for the existence of the dead layer.

RESULTS AND DISCUSSION

Figure 2a shows on-axis high-resolution X-ray diffraction (HR-XRD) $2\theta-\omega$ coupled scans of *t* nm Nd-doped SSO/10 nm SSO/GSO (110) where *t* was varied between 12 and 330 nm. The film at $t = 12$ nm revealed an expanded out-of-plane lattice parameter of 4.117 ± 0.002 Å, in agreement with the strain-stabilized tetragonal SSO polymorph on GSO (110).[14] This film also showed finite-size thickness fringes consistent with high structural quality and smooth surface morphology. With increasing *t*, films ($t = 26$ and 55 nm) showed an additional XRD peak corresponding to an orthorhombic phase.[14] It is noted that, although the two peaks for $t = 26$ nm are not apparent in the $(002)_{pc}$ (the subscript pc denotes pseudo-cubic) region of Figure 2a, the distinction is clearly visible in the $(103)_{pc}$ reciprocal space map (RSM) of Figure 3 (discussed below). With further increasing *t*, the tetragonal phase vanishes whereas the peak corresponding to the orthorhombic phase shifts toward higher 2θ values. Figure 2b shows the corresponding rocking curves as a function of *t*. These rocking curves can be described as a linear combination of two Gaussians (a narrow and a broad component).[17] This behavior is commonly seen in thin films where the narrow component reflects the low degree of structural disorder in coherent films, and the broad component reflects the disorder generated during strain relaxation.[27] We therefore plot $\frac{I_{broad}}{I_{broad} + I_{narrow}}$ as a function of *t* in Figure 2c to investigate the evolution of structural disorder with film thickness. Here, I_{broad} and I_{narrow} are the peak intensities of the broad and narrow Gaussian components, respectively. The value of $\frac{I_{broad}}{I_{broad} + I_{narrow}}$ was found to increase with *t* reaching a constant value of 1 for $t \geq 110$ nm, suggesting a higher structural disorder for thicker films. To this end, it is apparent that strain relaxation that is initiated via phase transition is accompanied by increasing structural disorder. It remains unclear, however, whether or not these phases relax via forming misfit dislocations at the substrate/film interface.

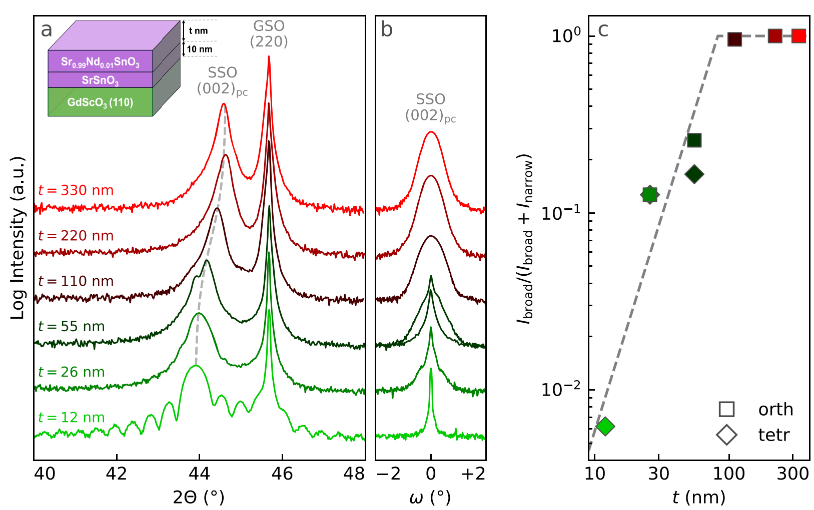

Figure 2. High-resolution X-ray diffraction coupled scans (a) and rocking curves (b) of *t* nm Nd-doped SSO/10 nm SSO/GSO. (c) $\frac{I_{broad}}{I_{broad} + I_{narrow}}$ as a function of *t*, where I_{broad} and I_{narrow} are the peak heights of the broad and narrow Gaussian components, respectively.

https://dx.doi.org/10.1021/acsaelm.0c00997
ACS Appl. Electron. Mater. 2021, 3, 1127−1132

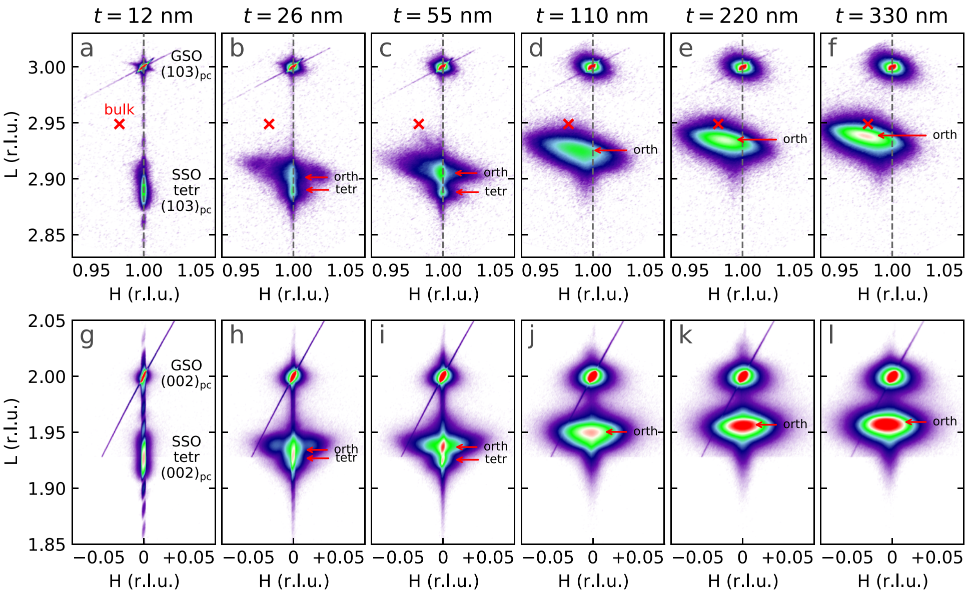

Figure 3. Thickness-dependent reciprocal space maps (RSMs). (a–f) Asymmetric RSMs around the $(103)_{pc}$ reflection and (g–l) symmetric RSMs around the $(002)_{pc}$ reflection for t nm Nd-doped SSO/10 nm SSO/GSO (110) as a function of t. The red arrow indicates Bragg peaks corresponding to two phases present in the film. The cross symbol indicates the position in the reciprocal space corresponding to the fully relaxed lattice parameter of SSO.

To investigate this question, we measured both in-plane and out-of-plane lattice parameters as a function of t. Figure 3 shows asymmetric RSMs around the $(103)_{pc}$ reflection (top panels) and symmetric RSMs around the $(002)_{pc}$ reflection (bottom panels) for t nm Nd-doped SSO/10 nm SSO/GSO (110) as a function of t. Consistent with the coupled scans, RSMs again confirmed the $T \rightarrow O$ transformation followed by a change in the lattice parameters. To illustrate this point, we show in Figure 4a the measured in-plane (a_{ip}) and out-of-plane (a_{op}) lattice parameters of both phases determined from the analysis of the RSMs as a function of t. Diamond and square symbols denote the tetragonal and orthorhombic phases, respectively. Figure 4a shows the emergence of the orthorhombic phase for $t \geq 26$ nm, and it reveals that both orthorhombic and tetragonal phases remain fully coherent to the GSO substrate up to t = 55 nm. Despite no change in a_{ip}, a_{op} of the orthorhombic phase was found to decrease whereas a_{op} of the tetragonal phase remained unchanged. At t = 110 nm, a partially relaxed orthorhombic phase was observed with no measurable tetragonal phase suggesting strain relaxation via the $T \rightarrow O$ transformation completes between 55 and 110 nm. The film then begins to relax by forming misfit dislocations accompanied by a change in lattice parameters reaching a bulk value of ~4.035 Å at t = 330 nm.[14,28]

We now discuss these lattice parameters in detail. At $t \geq 110$ nm, the orthorhombic phase undergoes a decrease in a_{op} accompanied by an increase in a_{ip}. This is an expected behavior from (compressive) strain relaxation owing to the formation of misfit dislocations. However, it may not be self-evident as to why the $T \rightarrow O$ transformation occurs when a_{ip} remains unchanged. This is contrary to expectations as the constraint on a_{ip} via coherent strain is understood to be the cause of the strain-stabilized tetragonal phase. However, here, it turns out that strain stabilization perishes while a_{ip} is still at its constrained value. Additionally, it was puzzling as to why the $T \rightarrow O$ transformation (for 26 nm $\leq t \leq$ 55 nm) is accompanied by a decrease in a_{op} only for the orthorhombic

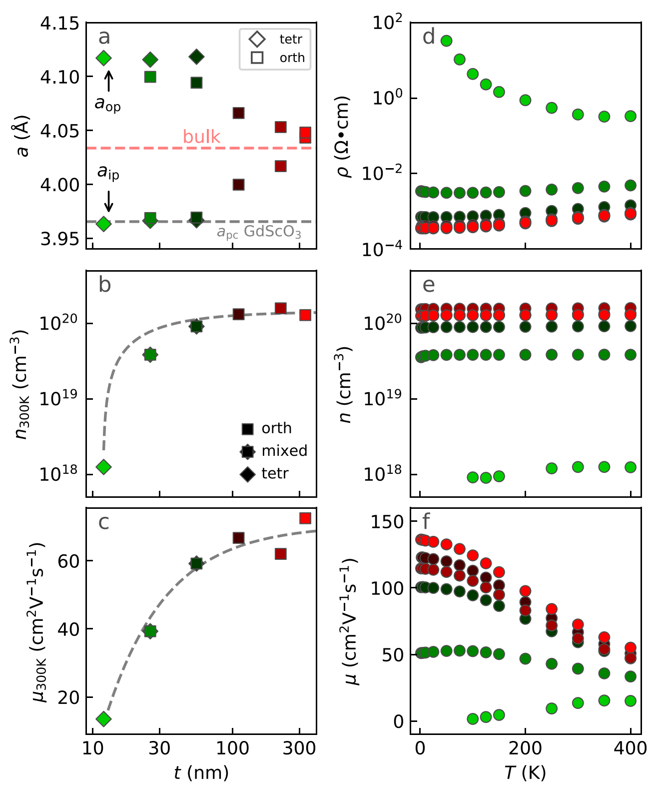

Figure 4. (a) In-plane (a_{ip}) and out-of-plane lattice parameter (a_{op}) of t nm Nd-doped SSO/10 nm SSO/GSO (110) as a function of t. (b, c) Room-temperature 3D electron density n_{300K} and mobility μ_{300K} versus t, respectively. (d–f) Resistivity (ρ), n_{3D}, and μ of these films, respectively, as a function of temperature.

phase whereas a_{ip} for both phases remains unchanged. To provide a qualitative explanation for this observation, we refer to Figure 1 and remind the reader that an epilayer undergoing symmetry ($T \rightarrow O$) relaxation is characterized by a coexistence of these two phases separated by vertical coherent phase boundaries.[29] Figure S1 shows a schematic of this spatial arrangement. When the epilayer is predominantly tetragonal with only small volume fractions of the orthorhombic phase (such as t = 26 nm, as shown in Figure 3c), all orthorhombic phases are directly adjacent to their tetragonal counterpart.[29] Therefore, a_{op} of the orthorhombic fraction is pinned to that of the tetragonal phase via a laterally directed coherent strain. This is similar to the strain mechanism operative in vertically aligned nanocomposites.[30] At larger thicknesses when less tetragonal phase is present (t = 55 nm, as shown in Figure 3d), the orthorhombic phase is separated from the tetragonal regions by an additional orthorhombic phase. In this case, laterally directed coherent strain relaxes, resulting in a decrease in a_{op} for the orthorhombic phase. However, why is the orthorhombic lattice parameter influenced by the tetragonal phase and not vice versa? We explain this again by referring to Figure 1, where we see that a_{op} for the tetragonal phase is fully defined by the length of Sn−O bonds that are colinear and oriented in the out-of-plane direction. For the orthorhombic phase, however, a_{op} is a function of both the Sn−O bond length and the octahedral rotation angles. Therefore, the orthorhombic phase can easily accommodate larger a_{op} by simply decreasing the angles of the a^+ or b^- rotations. Future investigations using transmission electron microscopy should be directed to investigate the laterally directed coherent strain relaxation process.

Finally, we discuss the effect of thickness and strain relaxation on electronic transport. Figure 4b and Figure 4c show room-temperature electron density (n_{300K}) and mobility (μ_{300K}) as a function of t, respectively. Both n_{300K} and μ_{300K} were found to increase from 1.3×10^{18} to 1.3×10^{20} cm^{-3} and from 14 to 67 cm^2 V^{-1} s^{-1}, respectively, between 12 and 110 nm and then become approximately independent of film thicknesses. Coincidently, this is the same thickness range in which strain relaxation was found to occur via the $T \rightarrow O$ transformation, raising the question what are the effects of phase fraction and phase boundary on electron density and mobility?

To investigate the increase in carrier density and mobility between 12 and 110 nm, we show in Figure S2 the n_{2D} as a function of t. In an uncompensated semiconductor, n_{2D} versus t should follow a straight line passing through the origin where the slope of the line yields n_{3D}. As expected, our experimental data showed a linear behavior but with a finite x-intercept. The slope yielded a 3D density of 1.4×10^{20} cm^{-3} consistent with the expected donor density based on the doping calibration. A finite x-intercept, however, suggests a conduction dead layer thickness of ∼11.8 nm, i.e., the film thickness over which electrons are fully compensated and do not contribute to conduction. A cause of the conduction dead layer in semiconductors can be the depletion effect from band bending due to charges at the surface. However, the 11.8 nm dead layer in this study would be extraordinarily large given our high donor density of $N_d = 1.4 \times 10^{20}$ cm^{-3}. In fact, assuming a relative permittivity value for SSO of $\varepsilon_r = 15$, this would correspond to a built-in surface potential of 12 V, which is inconceivable considering this would invert the valence band maximum well above the Fermi level at the surface. Therefore, the conduction dead layer in SSO cannot be explained by surface depletion alone. Rather, we hypothesize that it is due to the strong localization effect owing to surface or interface disorder in thin films. To this end, we performed temperature-dependent resistivity and Hall measurements of films as a function of t, as shown in Figure 4d−f, revealing a degenerate semiconductor metallic behavior for films $t \geq 26$ nm between 1.8 and 400 K. However, the thinnest film (t = 12 nm) yielded insulating behavior indicating the important role of strong localization in thinner films where t only slightly exceeds the conduction dead layer thickness. It is further noted that the increase in mobility with thickness is surprising given that the tetragonal phase is expected to possess higher electron mobility than the orthorhombic phase. This result thus further points to an important role of surface scattering in limiting the mobility of thinner SSO films. A future study will be directed to investigate this effect.

■ CONCLUSIONS

In summary, we have performed a systematic study of strain relaxation in the strain-stabilized tetragonal phase of Nd-doped SSO. It was found that strain relaxation occurs via the $T \rightarrow O$ phase transformation followed by relaxation via misfit dislocations. We also reveal various subtleties of the strain relaxation process including how the volume fraction of the two phases affects a_{op} of the orthorhombic phase via laterally directed coherent strain. Finally, we show that Nd-doped SSO has a conduction dead layer that cannot be explained by band bending alone, and we propose disorder-driven localization at the surface or interface as a potential explanation for the dead layer. This study provides an important step forward utilizing SSO as a new UWBG perovskite semiconductor for the development of high-power electronic devices.

■ METHODS

Samples were grown using a radical-based hybrid molecular beam epitaxy (MBE) approach.[14,31,32] A brief description of this approach is included here. All films were grown in an EVO 50 MBE system (Omicron, Germany). Substrates were heated to 950 °C (thermocouple temperature). Before growth, the substrates were cleaned for 20 min using radio frequency (RF) oxygen plasma (Mantis, UK) operating at 250 W and at an oxygen pressure of 5×10^{-6} Torr. Strontium (Sr) was supplied from a thermal effusion cell with a beam equivalent pressure (BEP) of 2.4×10^{-8} Torr. Tin was supplied via a gas injector (E-Science Inc.) using a radical-forming chemical precursor hexamethylditin (HMDT) at a BEP of 2×10^{-6} Torr. All films were grown in the presence of oxygen plasma operating at 250 W and at an oxygen pressure of 5×10^{-6} Torr. These growth conditions yielded a growth rate of 55 nm/h. For electrical measurements, films were doped n-type using neodymium (Nd). Nd was supplied from a thermal effusion cell operating at a fixed temperature of 940 °C.

Films were characterized using high-resolution X-ray diffraction (HR-XRD) and van der Pauw (VdP) Hall measurements. HR-XRD coupled scans and rocking curves were collected with an X'Pert Pro thin film diffractometer (PANalytical, Netherlands) equipped with a Cu parabolic mirror and Ge four-bounce monochromator. Lattice parameters were extracted from RSMs, which were collected with a SmartLab XE thin film diffractometer (Rigaku, Japan) collected with parallel-beam optics, a Ge two-bounce monochromator, and HyPix-3000 2D detector. Electrical measurements were performed in a physical property measurement system (DynaCool, Quantum Design, USA) using a VdP configuration. Indium was used to make ohmic metal contacts. Magnetic field and temperature were varied between ±9 T and 1.8−300 K respectively.

■ ASSOCIATED CONTENT

Supporting Information

The Supporting Information is available free of charge at https://pubs.acs.org/doi/10.1021/acsaelm.0c00997.

https://dx.doi.org/10.1021/acsaelm.0c00997
ACS Appl. Electron. Mater. 2021, 3, 1127−1132

A linear fit showing the thickness of the conduction dead layer (PDF)

AUTHOR INFORMATION

Corresponding Authors

Tristan K. Truttmann − *Department of Chemical Engineering and Materials Science, University of Minnesota − Twin Cities, Minneapolis, Minnesota 55455, United States*; Email: trutt009@umn.edu

Bharat Jalan − *Department of Chemical Engineering and Materials Science, University of Minnesota − Twin Cities, Minneapolis, Minnesota 55455, United States*; orcid.org/0000-0002-7940-0490; Email: bjalan@umn.edu

Authors

Fengdeng Liu − *Department of Chemical Engineering and Materials Science, University of Minnesota − Twin Cities, Minneapolis, Minnesota 55455, United States*

Javier Garcia-Barriocanal − *Characterization Facility, University of Minnesota − Twin Cities, Minneapolis, Minnesota 55455, United States*

Richard D. James − *Department of Aerospace Engineering and Mechanics, University of Minnesota − Twin Cities, Minneapolis, Minnesota 55455, United States*

Complete contact information is available at: https://pubs.acs.org/10.1021/acsaelm.0c00997

Author Contributions

T.K.T. and B.J. conceived the experiment. T.K.T. and F.L. grew the films. T.K.T., F.L., and J.G.-B. characterized the films. T.K.T., F.L., J.G.-B., R.D.J., and B.J. analyzed and interpreted the data and wrote the manuscript.

Notes

The authors declare no competing financial interest.

ACKNOWLEDGMENTS

This work was supported by the Air Force Office of Scientific Research (AFOSR) through Grant no. FA9550-19-1-0245 and through NSF DMR-1741801. The work also benefitted from the Norwegian Centennial Chair Program (NOCC) and a Vannevar Bush Faculty Fellowship. Parts of this work were carried out at the Minnesota Nano Center and Characterization Facility, University of Minnesota, which receives partial support from NSF through the MRSEC program under Award Number DMR-2011401.

REFERENCES

(1) Kim, H. J.; Kim, U.; Kim, T. H.; Kim, J.; Kim, H. M.; Jeon, B.-G.; Lee, W.-J.; Mun, H. S.; Hong, K. T.; Yu, J.; Char, K.; Kim, K. H. Physical properties of transparent perovskite oxides (Ba,La)SnO_3 with high electrical mobility at room temperature. *Phys. Rev. B* **2012**, *86*, 165205.

(2) Mizoguchi, H.; Eng, H. W.; Woodward, P. M. Probing the Electronic Structures of Ternary Perovskite and Pyrochlore Oxides Containing Sn^{4+} or Sb^{5+}. *Inorg. Chem.* **2004**, *43*, 1667.

(3) Prakash, A.; Quackenbush, N. F.; Yun, H.; Held, J.; Wang, T.; Truttmann, T.; Ablett, J. M.; Weiland, C.; Lee, T.-L.; Woicik, J. C.; Mkhoyan, K. A.; Jalan, B. Separating electrons and donors in $BaSnO_3$ via band engineering. *Nano Lett.* **2019**, *19*, 8920.

(4) Zhang, W.; Tang, J.; Ye, J. Structural, photocatalytic, and photophysical properties of perovskite $MSnO_3$ (M = Ca, Sr, and Ba) photocatalysts. *J. Mater. Res.* **2007**, *22*, 1859.

(5) Kim, H. M.; Kim, U.; Park, C.; Kwon, H.; Char, K. Thermally stable pn-junctions based on a single transparent perovskite semiconductor $BaSnO_3$. *APL Mater.* **2016**, *4*, No. 056105.

(6) Wang, J.; Luo, B. Electronic properties of p-type $BaSnO_3$ thin films. *Ceram. Int.* **2016**, *46*, 25678.

(7) Paik, H.; Chen, Z.; Lochocki, E.; Seidner, H. A.; Verma, A.; Tanen, N.; Park, J.; Uchida, M.; Shang, S.; Zhou, B.-C.; Brützam, M.; Uecker, R.; Liu, Z.-K.; Jena, D.; Shen, K. M.; Muller, D. A.; Schlom, D. G. Adsorption-controlled growth of La-doped $BaSnO_3$ by molecular-beam epitaxy. *APL Mater.* **2017**, *5*, 116107.

(8) Prakash, A.; Xu, P.; Faghaninia, A.; Shukla, S.; Ager, J. A., III; Lo, C. S.; Jalan, B. Wide bandgap $BaSnO_3$ films with room temperature conductivity exceeding 10^4 S cm^{-1}. *Nat. Commun.* **2017**, *8*, 15167.

(9) Mun, H.; Kim, U.; Min Kim, H.; Park, C.; Hoon Kim, T.; Joon Kim, H.; Hoon Kim, K.; Char, K. Large effects of dislocations on high mobility of epitaxial perovskite $Ba_{0.96}La_{0.04}SnO_3$ films. *Appl. Phys. Lett.* **2013**, *102*, 252105.

(10) Lee, W.-J.; Kim, H. J.; Sohn, E.; Kim, T. H.; Park, J.-Y.; Park, W.; Jeong, H.; Lee, T.; Kim, J. H.; Choi, K.-Y.; Kim, K. H. Enhanced electron mobility in epitaxial (Ba,La)SnO_3 films on $BaSnO_3$ (001) substrates. *Appl. Phys. Lett.* **2016**, *108*, No. 082105.

(11) Shiogai, J.; Nishihara, K.; Sato, K.; Tsukazaki, A. Improvement of electron mobility in La:$BaSnO_3$ thin films by insertion of an atomically flat insulating (Sr,Ba)SnO3 buffer layer. *AIP Adv.* **2016**, *6*, No. 065305.

(12) Guguschev, C.; Klimm, D.; Brützam, M.; Gesing, T. M.; Gogolin, M.; Paik, H.; Dittmar, A.; Fratello, V. J.; Schlom, D. G. Single crystal growth and characterization of Ba_2ScNbO_6 − A novel substrate for $BaSnO_3$ films. *J. Cryst. Growth* **2019**, *528*, 125263.

(13) Uecker, R.; Bertram, R.; Brützam, M.; Galazka, Z.; Gesing, T. M.; Guguschev, C.; Klimm, D.; Klupsch, M.; Kwasniewski, A.; Schlom, D. G. Large-lattice-parameter perovskite single-crystal substrates. *J. Cryst. Growth* **2017**, *457*, 137.

(14) Wang, T.; Prakash, A.; Dong, Y.; Truttmann, T.; Bucsek, A.; James, R.; Fong, D. D.; Kim, J.-W.; Ryan, P. J.; Zhou, H.; Birol, T.; Jalan, B. Engineering $SrSnO_3$ Phases and Electron Mobility at Room Temperature Using Epitaxial Strain. *ACS Appl. Mater. Interfaces* **2018**, *10*, 43802.

(15) Singh, D. J.; Xu, Q.; Ong, K. P. Strain effects on the band gap and optical properties of perovskite $SrSnO_3$ and $BaSnO_3$. *Appl. Phys. Lett.* **2014**, *104*, No. 011910.

(16) Ong, K. P.; Fan, X.; Subedi, A.; Sullivan, M. B.; Singh, D. J. Transparent conducting properties of $SrSnO_3$ and $ZnSnO_3$. *APL Mater.* **2015**, *3*, No. 062505.

(17) Truttmann, T.; Prakash, A.; Yue, J.; Mates, T. E.; Jalan, B. Dopant solubility and charge compensation in La-doped $SrSnO_3$ films. *Appl. Phys. Lett.* **2019**, *115*, 152103.

(18) Wang, T.; Thoutam, L. R.; Prakash, A.; Nunn, W.; Haugstad, G.; Jalan, B. Defect-driven localization crossovers in MBE-grown La-doped $SrSnO_3$ films. *Phys. Rev. Mater.* **2017**, *1*, No. 061601.

(19) Baba, E.; Kan, D.; Yamada, Y.; Haruta, M.; Kurata, H.; Kanemitsu, Y.; Shimakawa, Y. Optical and transport properties of transparent conducting La-doped $SrSnO_3$ thin films. *J. Phys. D: Appl. Phys.* **2015**, *48*, 455106.

(20) Wei, M.; Sanchela, A. V.; Feng, B.; Ikuhara, Y.; Cho, H. J.; Ohta, H. High electrical conducting deep-ultraviolet-transparent oxide semiconductor La-doped $SrSnO_3$ exceeding ∼ 3000 S cm^{-1}. *Appl. Phys. Lett.* **2020**, *116*, No. 022103.

(21) Chaganti, V. R. S. K.; Prakash, A.; Yue, J.; Jalan, B.; Koester, S. J. Demonstration of a Depletion-Mode SrSnO 3 n-Channel MESFET. *IEEE Trans. Electron Devices* **2018**, *39*, 1381.

(22) Rondinelli, J. M.; May, S. J.; Freeland, J. W. Control of octahedral connectivity in perovskite oxide heterostructures: An emerging route to multifunctional materials discovery. *MRS Bull.* **2012**, *37*, 261.

(23) Zheng, Y.; Wang, B.; Woo, C. H. Critical thickness for dislocation generation during ferroelectric transition in thin film on a compliant substrate. *Appl. Phys. Lett.* **2006**, *89*, No. 083115.

(24) Pompe, W.; Gong, X.; Suo, Z.; Speck, J. S. Elastic energy release due to domain formation in the strained epitaxy of ferroelectric and ferroelastic films. *J. Appl. Phys.* **1993**, *74*, 6012.
(25) Pertsev, N. A.; Tagantsev, A. K.; Setter, N. Phase transitions and strain-induced ferroelectricity in $SrTiO_3$ epitaxial thin films. *Phys. Rev. B* **2000**, *61*, R825.
(26) Choi, K. J.; Biegalski, M.; Li, Y. L.; Sharan, A.; Schubert, J.; Uecker, R.; Reiche, P.; Chen, Y. B.; Pan, X. Q.; Gopalan, V.; Chen, L.-Q.; Schlom, D. G.; Eom, C. B. Enhancement of Ferroelectricity in Strained $BaTiO_3$ Thin Films. *Science* **2004**, *306*, 1005.
(27) Miceli, P. F.; Palmstrøm, C. J. X-ray scattering from rotational disorder in epitaxial films: An unconventional mosaic crystal. *Phys. Rev. B* **1995**, *51*, 5506.
(28) Mountstevens, E. H.; Attfield, J. P.; Redfern, S. A. T. Cation-size control of structural phase transitions in tin perovskites. *J. Phys.: Condens. Matter* **2003**, *15*, 8315.
(29) Prakash, A.; Wang, T.; Bucsek, A.; Truttmann, T. K.; Fali, A.; Cotrufo, M.; Yun, H.; Kim, J.-W.; Ryan, P. J.; Mkhoyan, K. A.; Alù, A.; Abate, Y.; James, R. D.; Jalan, B. Self-Assembled Periodic Nanostructures Using Martensitic Phase Transformations. *Nano Lett.* **2021**, 1246.
(30) Zhu, B.; Schusteritsch, G.; Lu, P.; MacManus-Driscoll, J. L.; Pickard, C. J. Determining interface structures in vertically aligned nanocomposite films. *APL Mater.* **2019**, *7*, No. 061105.
(31) Prakash, A.; Xu, P.; Wu, X.; Haugstad, G.; Wang, X.; Jalan, B. Adsorption-controlled growth and the influence of stoichiometry on electronic transport in hybrid molecular beam epitaxy-grown $BaSnO_3$ films. *J. Mater. Chem. C* **2017**, *5*, 5730.
(32) Prakash, A.; Wang, T.; Choudhary, R.; Haugstad, G.; Gladfelter, W. L.; Jalan, B. Precursor selection in hybrid molecular beam epitaxy of alkaline-earth stannates. *J. Vac. Sci. Technol., A* **2020**, *38*, No. 063410.

https://dx.doi.org/10.1021/acsaelm.0c00997
ACS Appl. Electron. Mater. 2021, 3, 1127−1132